Numerical Identification of the Potential of Whisker- and Platelet-Filled Polymers

Andrei A. Gusev

Institute of Polymers, Department of Materials, ETH-Zentrum, CNB D93, Universitätsstrasse 6, 8092 Zürich, Switzerland

ABSTRACT: A generic finite-element based approach for predicting the behavior and properties of multiphase materials comprised of anisotropic, arbitrarily shaped and oriented phases is presented. The approach is exact in principle and effective in practice. It is the consistent use of periodic boundary conditions in the course of generating multiinclusion Monte Carlo configurations, dividing them into morphology−adaptive quality meshes, and numerical solution for the overall, effective properties that extracts an accurate prediction of the behavior and properties of multiphase materials from remarkably small computer models. The approach is employed to identify numerically the technological potential of some whisker- and platelet-filled polymers. It is demonstrated that the filled polymers studied have an appealing, currently unrealized technological potential. This potential has essentially been overlooked because of the widespread use of empirical equations tuned to reproduce available experimental data that unavoidably reflect the existing technological level.

Introduction

In the search for improved performance, the plastic industry is turning increasingly to the use of composite materials comprised of whiskers (carbon or glass fibers, rigid rodlike molecules, carbon nanotubes, cellulose whiskers, etc.) or platelets (talcum or bentonite minerals, clay or mica flakes, etc.) dispersed in a polymer matrix. Such filled polymers frequently offer a unique portfolio of technological properties unavailable with pure polymers, though one can still conveniently mold them into complex shapes with preexisting industrial equipment. Interestingly, for short-fiber-reinforced polymers alone, the rate of new papers registered by the Citation Database of the Institute for Scientific Information is rapidly approaching a level of a paper a day.[1]

The possibility of putting into polymers high-aspect-ratio nanosized objects, such as intercalated atomic thickness sheets of clay or mica, carbon nanotubes, silicon ladders, and cellulose whiskers, has further stimulated the interest in the field.[2−13] Because of their smallness, nano-objects can effectively be agitated by thermal motion that helps to evenly disperse them in a polymer. As a result, by loading just a few volume percent of such nano-objects into a polymer, one can significantly modify the mechanical, thermal, transport, electric, optical, and other properties. There are already existing applications of such nanocomposites, as well as many appealing expectations regarding their potential.

Theoretical prediction of the effective properties of composite materials from the constituents' properties and material's morphology has been a subject of extensive studies.[14] It is the rigorous variational bounds that should perhaps be viewed as the most firmly established theoretical means for predicting the effective properties of composites.[15−20] Among them, the outstanding Hashin−Shtrikman variational bounds[15,16] that have been exceedingly popular for nearly 4 decades. In general, the variational bounds deliver upper and lower margins on the effective properties of a composite. When the two bounds are tight, they can indeed be helpful. However, as the difference between the constituents' properties increases, the upper and lower bounds usually widen. Commonly, reinforcing whiskers and platelets are 2−6 orders of magnitude stiffer than the polymers. Such large difference makes the bounds' predictions practically useless for the design of whisker- and platelet-filled polymers.

Accurate rational models have been developed for predicting elastic, thermal, transport, and other properties of two-phase composites with spherical or infinitely long cylindrical inclusions.[14] However, for composites comprised of high aspect ratio whiskers and platelets, rational theoretical analysis has been limited to the domain of dilute filler concentrations, where one can effectively neglect the interactions between the inclusions.[21] Such diluted-regime theoretical models and their mean-field modifications can to some extent help to rationalize the properties of actual whisker- and platelet-filled materials, but one can hardly employ them reliably for design. As a result, various empirical equations, like that of Halpin and Tsai,[22,23] have commonly been employed for designing whisker- and platelet-filled materials.[24−26]

Empirical equations can no doubt successfully reproduce available experimental data, as the Halpin−Tsai equation does. However, both laboratory and industrial data unavoidably reflect the existing technological level, so the empirical approach does not suit intrinsically for deciding whether one can further improve the material's performance. Indeed, there are inevitable imperfections, including fiber and platelet agglomeration and their poor adhesion to the polymer. What is the degradation effect of these and other possible imperfections on the effective, composite properties? Clearly, such a question cannot be addressed with empirical equations designed and tuned to fit existing experimental data.

Numerical simulation techniques have now advanced to the point where it has become possible to envision the accurate prediction of the properties of whisker- and platelet-reinforced materials. This allows one to inspect the predictive capability of empirical equations by comparing their predictions with numerical results obtained with computer models with well-controlled morphology and phase properties. Moreover, because the empirical equations reflect the existing technological

10.1021/ma001979b CCC: $20.00
Published on Web 03/20/2001

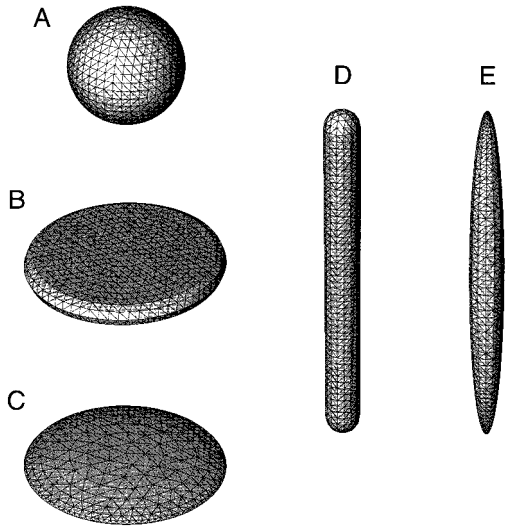

Figure 1. Geometric objects used in this work for numerical modeling of the behavior and properties of multiphase materials with particulate inclusions of various aspect ratios. The spherical object A has an aspect ratio of $a = 1$, while for the other objects $a = 10$. The visualization of the objects is achieved by using triangular surface meshes built on ca. 700 nodal points distributed over the objects' surfaces with a density proportional to the local curvature.

level, the difference between numerical and empirical predictions indicates what can be achieved by improving the existing technology, thus allowing one to identify the technological potential of the composite materials under consideration.

The goal of this paper is to present a finite-element-based approach allowing numerical identification of the technological potential of whisker- and platelet-filled materials from remarkably small periodic computer models. As applications, we consider the matching of the thermal expansion coefficients of a short-carbon-fiber-reinforced semicrystalline polymer with that of aluminum, incorporation of high-aspect ratio talcum flakes for improving the dimensional stability of a glassy polymer, and the use of biaxial drawing for manufacturing voided polymer films with a low dielectric constant.

Geometric Representation of High Aspect Ratio Inclusions

Figure 1 presents sketches of the geometric objects used in this work. For talcum platelets and chopped carbon fibers, we employ geometric objects made up of spherical and cylindrical sections (objects A, B, and D in Figure 1). However, such platelets and spherocylinders would be less appropriate for modeling the inclusions typical of many extruded or drawn multiphase materials, such as phase-separated polymer blends or rubber-toughened block copolymers. In these cases, the use of spheroidal objects (sketches C and E in Figure 1) would be more appropriate.

For numerical purposes, one approximates a geometric object by a set of discrete nodal points suitably situated on the object's surface. This set of surface nodes should accurately reproduce the object's shape but be reasonably modest regarding the total number of the nodes. To achieve this, we place the nodes onto the objects' surfaces with a density proportional to the local curvature of the surface. By using spherical or cylindrical coordinates, this can readily be accomplished for the objects made up of spherical, cylindrical, or flat surfaces (objects A, B, and D in Figure 1). However, one has to switch to a parametric representation to work out the problem for the objects with a smoothly varying surface curvature, such as spheroidal objects C and E in Figure 1.

Representative Multiinclusion Models

Typically, actual platelets and short fibers are of different size and shape. Furthermore, industrial short-fiber- and platelet-reinforced materials usually have a complex random microstructure in which the inclusions form an enormous variety of local microstructural arrangements. These two characteristics generally preclude the possibility of using one-inclusion models for predicting the behavior and properties of actual composites, thus confronting one with the necessity of using randomly packed multiinclusion models.

Such random models can be generated with a Monte Carlo technique (see Figure 2), starting from a regularly packed initial guess.[27] The Monte Carlo route also allows one to reliably account for available experimental details on the shape and size distribution of the inclusions and to incorporate into the computer model further morphological details, such as measured orientational distributions or spatial correlations in the mutual situations of the inclusions. This can be achieved by using available experimental morphology data for biasing the Monte Carlo runs.

A delicate problem, however, is to decide on the boundary conditions to use in the Monte Carlo runs. Indeed, forced to take a conservative perspective regarding the size of the computer models that can be studied numerically, one should immediately realize that, for relatively small randomly packed models comprised of high aspect ratio fibers or platelets, the presence of any external, open model's boundary would be unfavorable. Indeed, an attempt not to allow the inclusions to cross the model's boundary during a Monte Carlo run would lead to the appearance of a dummy matrix boundary layer, the presence of which could seriously corrupt the responses of small computer models. On the other hand, by cutting a small fragment from a much larger model, one could circumvent the above problem but would instead have difficulties in deciding, for example, how to deform the models when studying their mechanical behavior or how to apply the electric potential when studying the electrical properties. Should one use the same uniform boundary forces, displacements, or voltage regardless whether it is an inclusion or the matrix that appears in a particular section of the open, external model's boundary?

During the past decade, the problem of obtaining accurate predictions from small computer models has extensively been studied, both theoretically and numerically.[27−30] It has been demonstrated that it is periodic boundary conditions, a special class of mixed ones, that allows one to accurately predict the behavior and properties of multiphase materials from very small computer models.

Periodic Morphology-Adaptive Quality Meshes

The desire to consistently employ periodic boundary conditions in the numerical modeling of the behavior and properties of composite materials with random microstructure brings about the demand for periodic morphology−adaptive meshes. Here we intend to briefly discuss the principal stages involved in the generation

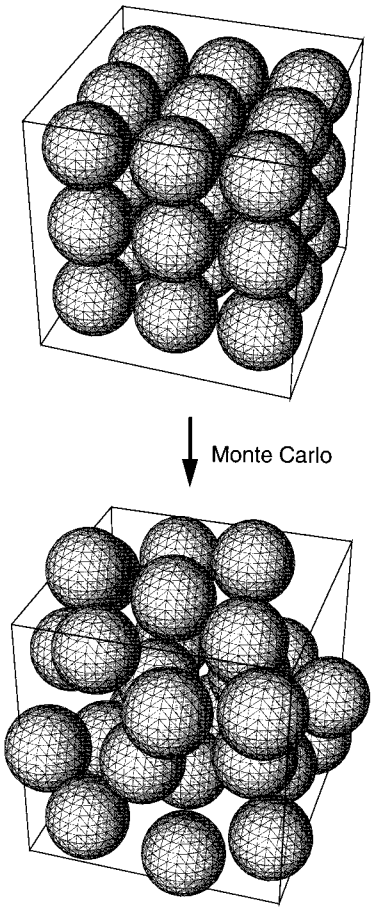

Figure 2. Monte Carlo route to the generation of periodic models for random composites. Here, starting from a regular cubic configuration of 27 identical spheres at a volume fraction of 0.5, we propagate the system through phase space by attempting small random displacements of the individual spheres. A new configuration is accepted provided that there is no overlap between the spheres. The Monte Carlo configurations generated in this way obey Percus−Yevick hard sphere statistics. It has already been shown, both theoretically (by using a micromechanics-based nonlocal constitutive equation) and numerically (by direct calculation of the elastic constants of periodic computer models with up to 64 nonoverlapping identical spheres) that the representative volume element size of this random elastic composite is remarkably small.[27,30] For the visualization of the spheres, we use triangular meshes built on ca. 250 nodes. These nodes were then used as a starting point for the generation of three-dimensional periodic morphology−adaptive meshes.

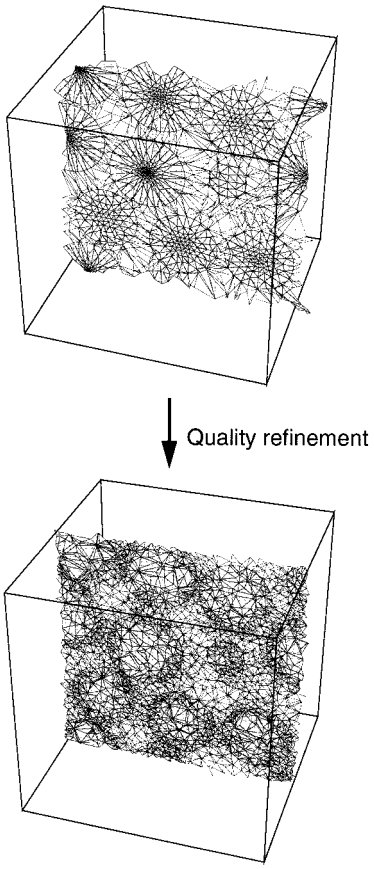

Figure 3. Periodic three-dimensional morphology−adaptive meshes for the random Monte Carlo configuration shown in Figure 2. The initial mesh consists of ca. 6×10^3 predefined surface shown as the nodes of the surface triangles in Figure 2 together with a cubic grid of $7 \times 7 \times 7$ nodes. This periodic mesh has ca. 36×10^3 tetrahedra. Note that the cross section of a plane cutting a tetrahedron can be of either triangular or quadrilateral shape. The quality mesh has a total of about 44×10^3 thousand nodes and 270×10^3 tetrahedra. From the 38×10^3 nodes added at the quality improvement stage, ca. 20×10^3 nodes were placed onto the inclusion's interfaces while the rest were placed at the circumcenters of the bridging tetrahedra and those with unsatisfactory quality.

of such meshes. Further methodological details and technicalities can be found elsewhere.[31−36] The reader is assumed to be familiar with Delaunay tessellation[32] and the sequential Bowyer−Watson algorithm widely employed for its computer generation.[33,33] For an introduction, consult recent surveys.[34−36]

Initial Periodic Mesh. After a Monte Carlo run, one can specify the positions of the interfaces separating the inclusions and the matrix. This gives a natural starting point for the generation of periodic meshes and the first stage is to place initial nodal points onto the inclusions' surfaces with a local density proportional to the local curvature of the inclusions' surfaces (see Figure 1). The next step is to mesh the surface nodes into a periodic Delaunay mesh of nonoverlapping tetrahedra covering space without holes.

In some cases, especially when dealing with computer models composed of a single inclusion, the starting set of surface nodal points is too unevenly distributed in space to allow the generation of a valid periodic mesh. To circumvent this problem, one places a regular grid of a few hundred nodal points inside the periodic box.[37] However, some of the regularly situated grid points can almost coincide with one or more already predefined surface nodes. This can cause problems in reproducing the system morphology in the final three-dimensional periodic mesh. To avoid this, we replace a grid point by its nearest predefined surface node whenever the two are separated by less than a certain distance.[37] Here we use regular grids of $7 \times 7 \times 7$ nodes with a replacement radius of $^1/_{10}$-th of the grid spacing.

Quality Improvement. After Delaunay triangulation of the predefined surface and grid nodes, one obtains a valid morphology−adaptive periodic mesh covering space without holes and overlaps between the tetrahedra. The problem is, however, that this initial mesh generally contains a large number of highly extended tetrahedra as well as those directly bridging two or even more inclusions (see Figure 3). The presence of such ill-favored tetrahedra does not allow one to obtain accurate numerical solutions for the effective properties, so one would like to get rid of them.

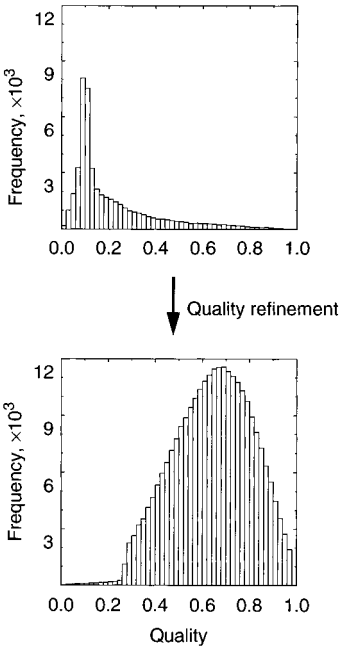

Figure 4. Quality improvement. The two distributions were calculated from the two periodic morphology−adaptive meshes sketched in Figure 3. On the horizontal axes, the relative element quality, i.e., the actual quality divided by that of an equisided tetrahedron, is plotted. The areas under the histograms give the number of the elements in the meshes.

The bridging tetrahedra can be removed by adding new nodes at the tetrahedra's circumcenters.[38] However, some mesh rearrangements can violate the morphology of the model, especially in the cases where the bridging tetrahedra connect closely situated surfaces of different inclusions. To prevent this from happening, we first carry out a distance-based refinement by inserting additional nodal points on those surface sections where the edges of tetrahedra's surface facets are large compared to the distance to the nearest surface of another inclusion.

We finally improve the mesh quality by inserting new nodes at the circumcenters of the tetrahedra of insufficient quality. The quality of a tetrahedron is defined as the ratio of its volume to the volume of its circumsphere. This quality measure is maximal for an equalsided tetrahedron. Importantly, the use of this quality measure allows one to reliably detect unwanted tetrahedra of poor shapes, including sliver-, cap-, needle-, and wedgelike tetrahedra.[36] Their presence can considerably slow the convergence of numerical calculations, so it is indeed strongly recommended to deal with meshes made up of high quality elements.

Figures 3 and 4 illustrate the quality refinement procedure for the random Monte Carlo configuration shown in Figure 2. One can see that both periodic meshes are truly periodic, and there are no additional boundary nodes placed on any external, opening planes that would commonly be present on the interiors whenever one attempted to mesh a periodic model with a structural, nonperiodic mesh generator. For relatively small periodic computer models, considering the scatter in the estimates obtained with differently situated opening planes, even a rational choice of such planes could become a nontrivial problem in its own right. Moreover, one would be confronted with the necessity of using additional, boundary nodes. Their presence can really become critical when dealing with periodic models of complex morphology where practically any opening plane could have some parts almost touching nearby sections of the internal model's interfaces. To reproduce these sections in the final mesh, one had to put many additional nodes onto these sections. In practice, the number of these additional nodes can quite often be exceedingly large.

By using consistently periodic mesh generators, such as the one presented in this work, one eludes in principle all the difficult problems arising when turning a periodic computer model into a solid body with open boundaries.

Implementation Details. An original in-house three-dimensional mesh generator was used in this work. In common with its two-dimensional predecessor,[31] this new mesh generator has also employed adaptive-precision floating-point arithmetic for the incircle and orientation tests.[39] However, it was programmed based on a different data-structure that allows one to implement a powerful cascade of mesh refinement operations. For example, when placing a new node onto the interface between an object and the matrix, the interface reconstruction was allowed, while the node insertions at the quality improvement stage were carried out under protection of the interfaces, i.e., rejecting the insertions destroying the interfaces. At the quality improvement stage, the mesh generator had a sustainable insertion performance clocked at about 5000 nodes a second on a single processor of a DEC AXP 8400 5/300 workstation.

Variational Formulations under Periodic Boundary Conditions

To calculate the effective properties of multiphase materials numerically, one should apply a certain perturbation to a computer model and then calculate its response. For example, to study electric properties, one should apply an external electric field and solve Laplace's equation for local nodal potentials. To study elastic responses, one should apply some effective strain or stress and then solve for nodal displacements. In the field of structural analysis, one can readily apply the perturbation to the structure's boundaries. Such boundaries are absent in the consistently periodic meshes required for accurate numerical predictions of the effective properties of multiphase materials. In this section, we present variational formulations allowing one to carry out numerical predictions of the effective properties of multiphase materials based on truly periodic meshes.

Laplace's Equation. There is a number of effective properties of multiphase materials that can be predicted by solving Laplace's equation. For example, the effective dielectric constants of a multiphase material can be obtained from the phase dielectric constants and material's morphology by solving Laplace's equation

$$\operatorname{div} \epsilon(\mathbf{r}) \operatorname{grad} \varphi = 0 \qquad (1)$$

where $\varphi = \varphi(\mathbf{r})$ is the local electric potential and $\epsilon = \epsilon(\mathbf{r})$ local dielectric constants. In general, both phase and effective dielectric constants are represented by second rank symmetric tensors. Equation 1 is also known as Poisson's equation of electrostatics. Table 1 reviews some technologically relevant physical properties governed by Laplace's equation. Further properties would include magnetic permeability, optical properties, etc. We refer the interesting reader to a very comprehensive review on the physical properties by Hale.[40]

Table 1. Some Effective Physical Properties Governed by Laplace's Equation[a]

phase property	local variable	Laplace's equation
dielectric constants, $\epsilon(\mathbf{r})$	electric potential, φ	div $\epsilon(\mathbf{r})$ grad $\varphi = 0$
thermal conductivity, $\lambda(\mathbf{r})$	temperature, T	div $\lambda(\mathbf{r})$ grad $T = 0$
electric conductance, $\sigma(\mathbf{r})$	electric potential, φ	div $\sigma(\mathbf{r})$ grad $\varphi = 0$
solute diffusion coeff, $D(\mathbf{r})$	concentration, c	div $D(\mathbf{r})$ grad $c = 0$
solute permeability, $P(\mathbf{r})$	chemical potential, μ	div $P(\mathbf{r})$ grad $\mu = 0$

[a] For multiphase materials with anisotropic constituents, the phase properties are given by second-rank symmetric 3 × 3 tensors.

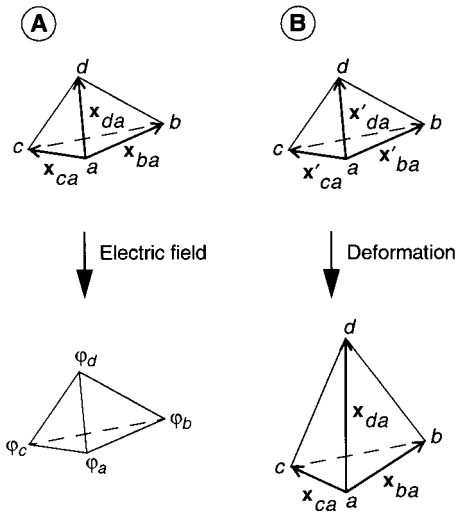

Figure 5. Element definition: (A) electrostatic problems; (B) elastostatic problems.

To solve Laplace's equation for the effective properties numerically, we take a variational perspective[41] and follow a displacement-based finite element route.[42] To be specific, we focus here on the formulation for the effective dielectric constants. As the degrees of freedom, we take nodal potentials φ_a. In this paper, the lower-case Latin subscripts a, b, c, and d denote the nodal points. The other lower-case Latin subscripts denote Cartesian coordinates and the Einstein summation convention applies to these Latin subscripts occurring twice in a product.

In the absence of a external electric field, all nodal potentials are assumed to be zero. When an external electric field $\mathbf{E}$ is applied, each node a generally acquires a nonzero potential φ_a. Assuming that the local polarization electric field $\mathbf{e}_\beta$ is constant inside tetrahedron β, one finds

$$\begin{aligned}\varphi_b - \varphi_a &= -x_{ba1}(e_{\beta1} + E_1) - x_{ba2}(e_{\beta2} + E_2) - x_{ba3}(e_{\beta3} + E_3)\\ \varphi_c - \varphi_a &= -x_{ca1}(e_{\beta1} + E_1) - x_{ca2}(e_{\beta2} + E_2) - x_{ca3}(e_{\beta3} + E_3)\\ \varphi_d - \varphi_a &= -x_{da1}(e_{\beta1} + E_1) - x_{da2}(e_{\beta2} + E_2) - x_{da3}(e_{\beta3} + E_3)\end{aligned} \quad (2)$$

where $\mathbf{x}_{ba}$, $\mathbf{x}_{ca}$, and $\mathbf{x}_{da}$ are three vectors defining the size and shape of tetrahedron β in the local frame with the origin at node a (see Figure 5). Equation 2 can be rewritten as

$$\Delta\varphi_{\beta i} = -h_{\beta ik}(e_{\beta k} + E_k) \quad (3)$$

where

$$h_{\beta ik} = [\mathbf{x}_{ba}, \mathbf{x}_{ca}, \mathbf{x}_{da}] = \begin{bmatrix} x_{ba1} & x_{ba2} & x_{ba3} \\ x_{ca1} & x_{ca2} & x_{ca3} \\ x_{da1} & x_{da2} & x_{da3} \end{bmatrix} \quad (4)$$

is the scaling matrix of tetrahedron β. From eq 3 one finds

$$e_{\beta i} + E_i = -h_{\beta ik}{}^{-1}\Delta\varphi_{\beta k} \quad (5)$$

where $h_{\beta ik}{}^{-1}$ is inverse of $h_{\beta ik}$.

The total electrical energy U is defined as

$$U \equiv \sum_\beta u_\beta = \frac{1}{8\pi}\sum_\beta V_\beta \epsilon_{\beta ik}(E_i + e_{\beta i})(E_k + e_{\beta k}) \quad (6)$$

where u_β is the electrical energy of tetrahedron β, V_β is its volume, $\epsilon_{\beta ik}$ are the dielectric constants inside tetrahedron β, E_i is the external field, and $e_{\beta i}$ is the polarization electric field inside tetrahedron β. From eqs 2−6, one concludes that the total energy U is a quadratic function of the N nodal potentials φ_a

$$U = U(\varphi_1, \varphi_2, ..., \varphi_N) = \frac{1}{2}\sum_{a,b}\varphi_a K_{ab}\varphi_b + \sum_a b_a\varphi_a + C \quad (7)$$

where K_{ab} is a symmetric $N \times N$ system Hessian matrix, b_a the force vector, and C a constant

$$K_{ab} \equiv \frac{\partial^2 U}{\partial\varphi_a\partial\varphi_b} \qquad b_a \equiv \frac{\partial U}{\partial\varphi_a}\Big|_0 \qquad C \equiv U|_0 \quad (8)$$

where $|_0$ means that all nodal potentials φ_a are set to zero. From eqs 6−8 one finds

$$K_{ab} = \frac{1}{4\pi}\sum_\beta V_\beta \frac{\partial e_{\beta i}}{\partial\varphi_a}\epsilon_{\beta ik}\frac{\partial e_{\beta k}}{\partial e\varphi_b} \quad b_a = \frac{1}{4\pi}\sum_\beta V_\beta E_i \epsilon_{\beta ik}\frac{\partial e_{\beta k}}{\partial\varphi_a}$$
$$C = \frac{1}{8\pi}\sum_\beta V_\beta E_i \epsilon_{\beta ik} E_k \quad (9)$$

where the geometric terms $\partial e_{\beta i}/\partial\varphi_a$ are formed by the components of the inverse scaling matrix $h_{\beta ik}{}^{-1}$ of tetrahedron β, as defined by eq 5.

Equation 9 shows that both the system Hessian matrix and the energy gradient can be assembled from those of the individual tetrahedra. One can also see that the system Hessian matrix does not depend on the external electric field applied, so it is the force vector and the constant term that entirely accumulate the dependence on the external field applied.

For a given periodic mesh and a particular external electric field applied, the total electric energy U has a unique minimum defined by a certain set of nodal potentials. At this minimum, the local polarization fields $\mathbf{e}_\beta$ inside the tetrahedra are uniquely defined by eq 5, so one can readily evaluate the effective electric induction $\mathbf{D}$ as

$$D_i = \sum_\beta V\epsilon_{\beta ik}(E_k + e_{\beta k}) \quad (10)$$

The effective dielectric constants $\langle\epsilon\rangle_{ik}$ are defined as

$$D_i = \langle\epsilon\rangle_{ik}E_k \quad (11)$$

so the six independent components of symmetric $\langle\epsilon\rangle_{ik}$

can generally be obtained in three independent minimization runs carried out under three different external fields **E**.

As eqs 2 and 7 indicate, we have separated the electric fields inside the tetrahedra into two separate contributions, namely the external spatially uniform field, **E**, and a local, spatially varying, polarization field, $\mathbf{e}_\beta$. This allows one to apply the external electric field **E** in the thermodynamic sense, i.e., inside the tetrahedra, thus avoiding the necessity of applying any boundary nodal potentials.

Elastostatic Problems. Here we present a linear elastostatic variational formulation under periodic boundary conditions. Its implementation was validated by comparing three-dimensional numerical predictions with ultrasonic measurements carried out on well-characterized laboratory samples.[43] A geometrically nonlinear formulation has already been presented elsewhere.[27]

The reference-state scaling matrix of tetrahedron β, i.e., the one before the deformation, is defined as (see Figure 5):

$$h'_{\beta ik} = [\mathbf{x}'_{ba}, \mathbf{x}'_{ca}, \mathbf{x}'_{da}] = \begin{bmatrix} x'_{ba1} & x'_{ca1} & x'_{da1} \\ x'_{ba2} & x'_{ca2} & x'_{da2} \\ x'_{ba3} & x'_{ca3} & x'_{da3} \end{bmatrix} \quad (12)$$

where $\mathbf{x}'_a$ is the position of node a before the deformation and $\mathbf{x}'_{ba} = \mathbf{x}'_b - \mathbf{x}'_a$. Throughout this paper, a primed entity stands for the entity value before the deformation.

During the deformation, each node a is generally displaced $\mathbf{x}'_a \rightarrow \mathbf{x}_a$ and one defines the scaling matrix of the deformed tetrahedron β as

$$h_{\beta ik} = [\mathbf{x}_{ba}, \mathbf{x}_{ca}, \mathbf{x}_{da}] \quad (13)$$

We assume that the local strain is constant inside the tetrahedra and define the displacement $\Delta\mathbf{r}$ at point **r** inside tetrahedron β as

$$\Delta r_i \equiv r_i - r'_i = (h_{\beta il} {h'_{\beta lm}}^{-1} - \delta_{\mathrm{im}}) r'_m \quad (14)$$

The deformation gradient inside tetrahedron β is then

$$\frac{\partial \Delta r_i}{\partial r'_k} = h_{\beta il} {h'_{\beta lk}}^{-1} - \delta_{ik} \quad (15)$$

where δ_{ik} is the Kronecker tensor. The local linear strain $e_{\beta ik}$ inside tetrahedron β is defined as

$$e_{\beta ik} = \frac{1}{2}\left(\frac{\partial \Delta r_i}{\partial r'_k} + \frac{\partial \Delta r_k}{\partial r'_i}\right) = \frac{1}{2}(h_{\beta il} {h'_{\beta lk}}^{-1} + h_{\beta kl} {h'_{\beta li}}^{-1}) - \delta_{ik} \quad (16)$$

The local strain $e_{\beta ik}$ is a symmetric second rank tensor with six independent components that are uniquely defined by the element's scaling matrices before and after the deformation.

Before the deformation the system shape and size are characterized by three continuation vectors $\mathbf{A}'$, $\mathbf{B}'$, and $\mathbf{C}'$, so we define the system scaling matrix of the undeformed system as

$$H'_{ik} = [\mathbf{A}', \mathbf{B}', \mathbf{C}'] \quad (17)$$

The effective strain is imposed by changing the reference-state continuation vectors

$$\mathbf{A}' \rightarrow \mathbf{A} \quad \mathbf{B}' \rightarrow \mathbf{B} \quad \mathbf{C}' \rightarrow \mathbf{C} \quad (18)$$

so after the deformation the system scaling matrix becomes

$$H_{ik} = [\mathbf{A}, \mathbf{B}, \mathbf{C}] \quad (19)$$

These two system scaling matrices define, through eqs 15 and 16, the effective strain E_{ik} imposed on the system

$$E_{ik} = \frac{1}{2}(H_{il} {H'_{lk}}^{-1} + H_{kl} {H'_{li}}^{-1}) - \delta_{ik} \quad (20)$$

Scaled coordinates s_{ai} are introduced via

$$x_{ai} = H_{ik} s_{ak} \quad (21)$$

The latter can be written as

$$x_{ai} = (H'_{ik} + \Delta H_{ik})(s'_{ak} + \Delta s_{ak}) = x'_{ai} + H'_{ik}\Delta s_{ak} + \Delta H_{ik} s'_{ak} + \Delta H_{ik}\Delta S_{ak} \quad (22)$$

where $\Delta H_{ik} = H'_{ik} - H_{ik}$ is the change in the system scaling matrix due to the effective strain imposed on the system. The last term on the right is of quadratic nature, and one should therefore neglect it within the linear elastic formulation.[44] The second term on the right describes spatially nonuniform displacements occurring without any effective deformation of the system, while the third term represents the displacements involved in homogeneous, spatially uniform affine deformations arising as $H'_{ik} \rightarrow H_{ik}$. Accordingly, within the linear elastic formulation considered, one can uniquely decompose the local linear strain defined by eq 16 into two separate contributions

$$e_{\beta ik} = e'_{\beta ik} + E_{ik} \quad (23)$$

where $e'_{\beta ik}$ and E_{ik} represent the spatially nonuniform and affine parts of the local strain, respectively, with the latter being given by eq 20.

The total strain energy U is defined as a sum over the tetrahedra

$$U = \sum_\beta u_\beta = \sum_\beta \frac{1}{2} V_\beta C_{\beta iklm}(e'_{\beta ik} + E_{ik} - e_{\beta ik}{}^T)(e'_{\beta lm} + E_{ik} - e_{\beta lm}{}^T) \quad (24)$$

where u_β is the strain energy of tetrahedron β, V_β its volume, $C_{\beta iklm}$ the elastic constants of the material inside tetrahedron β, and $e_{\beta ik}{}^T$ a local nonmechanical strain introduced here to account for a possible temperature change, shrinkage caused by the curing, or solvent uptake that may accompany the deformation.

Because of the linear elastic formulation, the total strain energy is a quadratic function of the scaled displacements $\Delta s_\zeta \equiv s_{ai} - s'_{ai}$, where $\zeta = 3a - i + 1$. We consider the $3N$ scaled displacements Δs_ζ as the degrees of freedom and write the total strain energy as follows:

$$U = U(\Delta\mathbf{s}_1, \Delta\mathbf{s}_2, ..., \Delta\mathbf{s}_N; H_{ik}) = \frac{1}{2}\sum_{\zeta,\eta} \Delta s_\zeta K_{\zeta\eta} \Delta s_\eta + \sum_\zeta b_\zeta \Delta s_\zeta + C \quad (25)$$

The global indices ζ and η run over the $3N$ degrees of

freedom, $K_{\zeta\eta}$ is the system Hessian matrix, b_ζ is the system force vector, and C is a constant.

The total strain energy of eq 24 is a sum of the element contributions. Therefore, the system Hessian matrix can also be written as a sum over the elements [compare with eq 9]:

$$K_{\zeta\eta} \equiv \frac{\partial^2 U}{\partial \Delta s_\zeta \partial \Delta s_\eta} = \frac{\partial^2 \sum_\beta u_\beta}{\partial \Delta s_\zeta \partial \Delta s_\eta} = \sum_\beta V_\beta \frac{\partial e'_{\beta ik}}{\partial s_\zeta} C_{\beta iklm} \frac{\partial e'_{\beta lm}}{\partial s_\eta} = \sum_\beta \kappa_{\beta\zeta\eta} \quad (26)$$

The element stiffness matrixes $\kappa_{\beta\zeta\eta}$ are 12 × 12 symmetric matrices with constant coefficients that are uniquely determined by the components of the element's scaling matrix $h'_{\beta ik}$ before the deformation and the elastic constants $C_{\beta iklm}$ of the material inside element β. The $\kappa_{\beta\zeta\eta}$ values depend neither on the scaled displacements Δs_ζ nor on the effective strain applied. Therefore, for a given periodic system, the $K_{\zeta\eta}$ matrix need be assembled only once. After this, one can use it without modification for studying the system's elastic response under an arbitrary combination of effective mechanical and nonmechanical strains.

From eq 25, the force vector b_ζ is the energy gradient at zero displacements:

$$b_\zeta \equiv \nabla_\xi U|_{\Delta \mathbf{s}=0} = \sum_\beta V_\beta (e'_{\beta ik} + E_{ik} - e_{\beta ik}{}^T) C_{\beta iklm} \frac{\partial e'_{\beta lm}}{\partial s_\eta} = \sum_\beta \nabla_\zeta u_\beta \quad (27)$$

In contrast to the system Hessian matrix, the force vector does depend on the effective mechanical strain E_{ik} and nonmechanical strains $e_{\beta ik}{}^T$. Therefore, for each combination of the mechanical and nonmechanical perturbations, one should carry out a separate assembly of the force vector. The only formal difference between these two parts of the effective strain is that the mechanical strain is acting uniformly while the nonmechanical ones may generally vary between the phases.

The constant term C is the strain energy of the deformed system at zero scaled displacements:

$$C \equiv U|_{\Delta \mathbf{s}=0} \quad (28)$$

Similar to the force vector b_ζ, the constant term C depends on the E_{ik} and $e_{\beta ik}{}^T$ components.

Likewise to the above formulation for Laplace's equation, it is the force vector b_ζ and the constant term C that depend on the external perturbation to which the periodic system is subjected. As a result, one can apply the effective mechanical E_{ik} and nonmechanical $e_{\beta ik}{}^T$ strains in a thermodynamic way, i.e., by using neither prescribed boundary nodal forces nor displacements.

For a given periodic mesh and a particular combination of the effective mechanical and nonmechanical strains imposed, the total strain energy U has a unique minimum defined by a certain set of nodal displacements. At the minimum, the local strains $e_{\beta ik}$ inside the tetrahedra are defined by eq 16, allowing one to evaluate the effective stress

$$\Sigma_{ik} \equiv \langle \sigma_{\beta ik} \rangle = \sum_\beta V_\beta C_{\beta iklm} e_{\beta lm} \quad (29)$$

where $\langle \sigma_{\beta ik} \rangle$ denotes the average local stress.

The effective elastic constants $\langle C \rangle_{iklm}$ can be calculated from the linear response equation

$$\Sigma_{ik} = \langle C \rangle_{iklm} E_{lm} \quad (30)$$

where E_{lm} is the effective mechanical strain imposed. In general, the 21 independent components of $\langle C \rangle_{iklm}$ can be obtained in six independent minimization runs conducted under six different effective strains E_{ik}.

To evaluate the effective thermal expansion coefficients $\langle \alpha \rangle_{ik}$, one applies local nonmechanical strains $e_{\beta ik}{}^T = \alpha_{\beta ik}$ corresponding to a temperature change of one degree and, assuming a zero effective mechanical strain E_{ik}, carries out the energy minimization. From the effective thermal stress $\Sigma_{lm}{}^T$ at the minimum, by using the equivalence of the thermal and elastic problems,[14] one finds

$$\langle \alpha \rangle_{ik}, = \langle C \rangle_{iklm}{}^{-1} \sum_{lm}{}^T \quad (31)$$

In a similar way, one can evaluate the effective swelling coefficients and the effective shrinkage caused, for example, by a chemical reaction or the relaxation of residual stresses occurring in one or more composite's constituents.

Solution

Both the Laplace and the elastostatic linear-response periodic formulations just presented lead to quadratic forms; see eqs 7 and 25. In both cases, the external perturbations, i.e., the external electric field and the effective strains, are incorporated into the linear (force) and constant terms. Our goal is, therefore, to find a set of nodal degrees of freedom minimizing these quadratic forms under a given external perturbation. As the resulting quadratic forms have constant coefficients, the minimum is unique.

To find this minimum in the space of system's degrees of freedom, and thus to solve the problem numerically, we use conjugate gradient minimization. This iterative minimization technique constructs a set of successive points that gradually converge to the minimum.[45] Technically, at each iteration, conjugate gradient minimization requires the gradient evaluation at the current point. For small and moderately large systems, when the computer has enough memory to store all the components of the sparse system Hessian matrix, the gradient can readily be evaluated as

$$\nabla_\zeta U = \sum_\beta K_{\zeta\eta} \Delta s_\eta + b_\zeta \quad (32)$$

The multiplication involved in eq 32 is carried out in the compressed sparse row format.[45] This route to the gradient evaluation is remarkably effective, but for big systems (e.g., with a million or more degrees of freedom for the elastostatic problems), the memory requirements become too great. In this situation one must switch to a direct evaluation of the system gradient.[27,42] This alternative requires much less memory but is not as fast.

In this work we have taken the faster route, together with Jacobi's diagonal preconditioning for the system Hessian matrix. All calculations presented below were

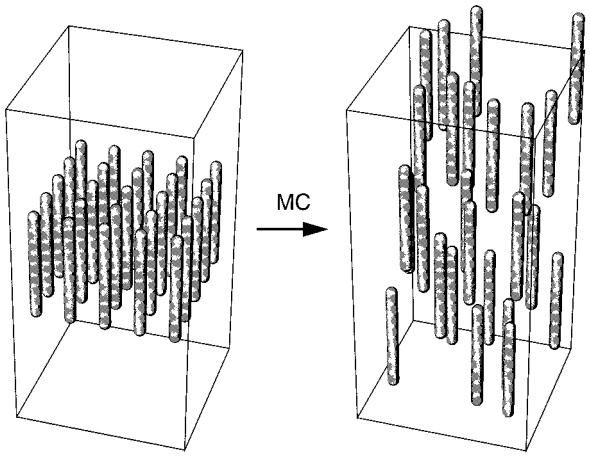

Figure 6. Generation of orthorhombic periodic computer models with 25 randomly dispersed identical parallel fibers. Here, the fiber aspect ratio is $a = 10$, and the fiber volume fraction $f = 0.03$.

carried out with in-house solvers on a single processor of a DEC AXP 8400 5/300 workstation. Typically, for periodic systems with a few hundred thousand nodal points, the conjugate gradient minimization required a few dozen CPU minutes for Laplace's solver, and a few CPU hours for the elastostatic one.

Short Carbon Fiber Reinforced Polymers

Computer Models. We have studied thermoelastic properties of a polymer reinforced by a random dispersion of perfectly aligned identical cylindrical fibers. The periodic computer models comprised 1, 4, 9, 16, and 25 identical spherocylinders (object D of Figure 1) with aspect ratios varying from 1 to 200. Periodic boundary conditions given by an orthorhombic box with two equal lateral dimensions were used (see Figure 6). For a model with a single fiber, the box and fiber aspect ratios were made equal. For a model with N fibers, the lateral box dimensions were increased by a factor of $\sqrt{N}$.

To generate a random model, the fibers were placed on a regular grid and a Monte Carlo run of a few million steps was started under orthorhombic periodic boundary conditions. The fiber orientations were kept constant during the Monte Carlo run. The final Monte Carlo configuration was meshed into a periodic mesh of nonoverlapping tetrahedra. A typical periodic morphology−adaptive quality mesh of a model with 25 fibers is shown in Figure 7.

For the fibers, we assumed thermoelastic properties of H370 carbon fibers: a longitudinal Young's modulus of $E_{33} = 370$ GPa and a transverse one of $E_{11} = 12$ GPa, Poisson's ratios $\nu_{12} = 0.48$ and $\nu_{13} = 0.35$, shear modulus $G_{13} = 17.5$ GPa, and thermal expansion coefficients of $\alpha_{33} = -1 \times 10^{-6}$ 1/K and $\alpha_{11} = 2.5 \times 10^{-5}$ 1/K. Because of the fiber symmetry, the five elastic moduli and two thermal expansion coefficients formed a complete set sufficient for describing an arbitrary thermoelastic response. For the matrix, we assumed some typical properties of an isotropic semicrystalline polymer, such as nylon 6 or polypropylene: $E = 1$ GPa, $\nu = 0.4$, and $\alpha = 1 \times 10^{-4}$ 1/K.

Representative Volume Element Size. As the number of fibers $N \rightarrow \infty$, numerical estimates should gradually level off approaching the values pertaining to large laboratory samples. The problem is however to decide on a minimal representative volume element

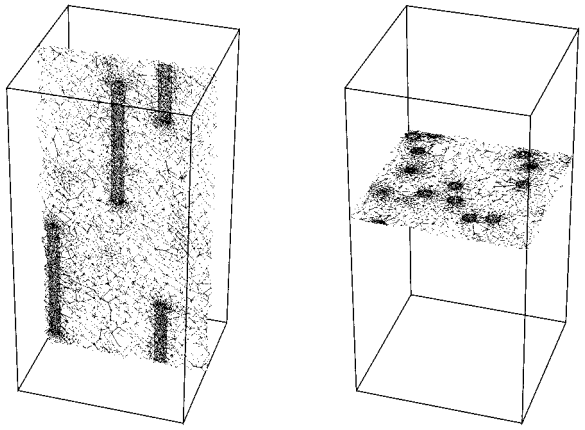

Figure 7. Periodic morphology−adaptive quality mesh used in this work for the random configuration sketched in Figure 6. The mesh had about 6×10^4 nodes and 4×10^5 tetrahedra.

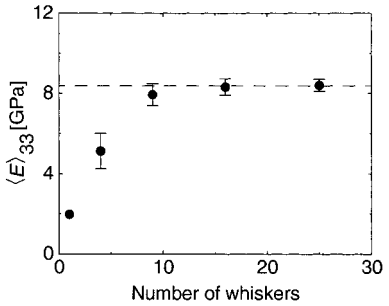

Figure 8. Approaching the uniform RVE size for the effective longitudinal Young's modulus $\langle E \rangle_{33}$. The fiber volume fraction is $f = 0.03$, and the aspect ratio $a = 100$. The average values shown by the solid circles and the error bars were estimated based on numerical results obtained with three independent computer models generated for each particular number of fibers studied. The dashed line was drawn through the average obtained with 25 fibers. The maximal stiffness that can be obtained at $f = 0.03$ as $a \rightarrow \infty$ is about 12 GPa, thus coinciding with the top of the plot.

(RVE) size, allowing one to obtain realistic predictions for the system of interest. For a composite comprised of a random dispersion of spherical inclusions, there is both theoretical and numerical evidence that the RVE size is remarkably small.[27,30] The question is, however, open for short-fiber-reinforced composites, and here we are specifically interested in the RVE size for the effective longitudinal Young's modulus $\langle E \rangle_{33}$.

It was found, in a series of numerical calculations illustrated in Figure 8, that random computer models with 16 and more fibers already delivered rather accurate estimates for $\langle E \rangle_{33}$. Contrary expectations, numerical estimates obtained with 4 randomly situated fibers were significantly below those obtained assuming 16 or more fibers. This leads one to question the adequacy of various popular empirical equations tuned to reproduce numerical results considering only one or a few regularly-situated fibers.[23,26]

Comparison with the Halpin−Tsai Equation. The Halpin−Tsai equation for predicting the effective properties of composite materials has been an industrial standard for nearly 3 decades.[22,23,26] For the effective longitudinal Young's modulus $\langle E \rangle_{33}$ of short-fiber-reinforced composites, the Halpin−Tsai equation states

$$\frac{\langle E \rangle_{33}}{E_m} = \frac{1 + 2a\eta f}{1 - \eta f} \quad \text{with } \eta = \frac{E_f/E_m - 1}{E_f/E_m + 1} \qquad (33)$$

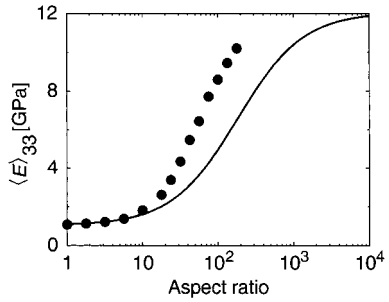

Figure 9. Comparison of numerical and Halpin−Tsai's predictions for the effective longitudinal Young's modulus, $\langle E \rangle_{33}$, of a short-carbon-fiber-reinforced composite with perfectly aligned fibers. The solid circles show numerical predictions collected with computer models of 16 randomly situated perfectly aligned fibers. The solid line gives the Halpin−Tsai predictions. The fiber volume fraction is $f = 0.03$.

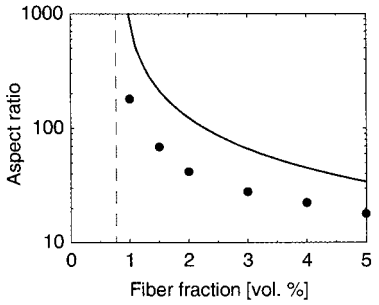

Figure 10. Design curve for the longitudinal thermal expansion coefficient, $\langle \alpha \rangle_{33}$, of a short-carbon-fiber-reinforced polymer. The fibers are assumed to be perfectly aligned. The design goal is to obtain the same effective $\langle \alpha \rangle_{33}$ as that of aluminum, i.e., 2.5×10^{-5} 1/K. Numerical predictions are shown by solid circles. They were obtained from calculated $\langle \alpha \rangle_{33}$ aspect-ratio dependences at different fixed fiber volume fractions, similar to the one shown for $\langle E \rangle_{33}$ in Figure 9. The solid line gives the Halpin−Tsai predictions. They were calculated from the Halpin−Tsai predictions for five independent effective elastic moduli,[23,26] based on the equivalence of the thermal and mechanical problems and available closed-form analytical solution for $\langle \alpha \rangle_{33}$ of a two-phase fiber-symmetry composite. The vertical dashed line shows what can be obtained with infinitely long fibers, i.e., with continuous-fiber unidirectional composites.

where E_m is the matrix Young's modulus, E_f is the longitudinal E_{33} modulus of the fibers, f is the fiber volume fraction, and a is the fiber aspect ratio. For $a = 1$ and $a \to \infty$, the Halpin−Tsai equation reproduces, within engineering accuracy, most theoretical results obtained with the "rational" composite and three-phase composite models proposed for composites of spherical inclusions or infinitely long, continuous fibers.[14,23]

For short-fiber-reinforced composites, the factor $2a$ present in eq 33 was empirically assigned based on experimental data available for a composite of short nylon fibers dispersed in a rubber matrix.[23] Real composites are seldom perfect as, for example, fiber agglomeration, misalignment, or poor adhesion between the fibers and the matrix influence the composite's performance. Additionally, some two-dimensional numerical data collected assuming regular fiber arrangements were employed for validation of eq 33. However, as we have just seen in the previous section, the RVE size for short-fiber-reinforced composites is rather large, so the regular computer models may deliver poor estimates for the reinforcement effect.

Figure 9 compares numerical predictions obtained in this work with the Halpin−Tsai ones. One can see that for small aspect ratios, e.g., up to $a \approx 10$, the Halpin−Tsai equation faithfully reproduces numerical results. However, at these small aspect ratios, the reinforcing effect is practically absent. Disappointingly, for moderate aspect ratios between 10 and 1000, the Halpin−Tsai equation does not render any realistic prediction. In practice, this domain of moderate fiber aspect ratios is technologically the most significant one.

Putting Nanotubes into Polymers. When molded into complex shapes, carbon fibers dispersed in a polymer are usually chopped during the processing resulting in a maximal aspect ratio only of about 100.[3] The Halpin−Tsai equation predicts (see Figure 9) that with such chopped fibers one can realize only about a third of the maximal performance. Therefore, it is commonly believed that one should work with carbon fibers of an aspect ratio of at least 1000 to make significantly stiff materials.[3] Nanotubes can have aspect ratios of 1000 and more, attracting lately much attention as potential high-aspect-ratio fillers, despite their currently absurd cost of roughly 10 times the price of gold.[2,3]

Maximal reinforcement can obviously be obtained with continuous fibers, i.e., as $a \to \infty$. The problem is, however, to understand at which fiber aspect ratio one can realize, say, 80% of this maximal performance. For the carbon-fiber-filled polymer studied, the Halpin−Tsai equation predicts this point out at $a \approx 800$, providing a rather gloomy perspective for carbon-fiber-reinforced polymers. On the contrary, the numerical predictions are much more optimistic, indicating that at $a \approx 100$ one can already realize about 80% of the maximal reinforcement (see Figure 9).

Matching the Thermal Expansion of Short-Carbon-Fiber-Reinforced Polymers and Metals. In many demanding applications, including aviation, aerospace, and the automobile industry, one is interested in lowering the mismatch between the thermal expansion of metals and polymer-based composite materials. Typically, organic polymers have a linear thermal expansion α of about 10^{-4} 1/K, while for metals $\alpha \approx 10^{-5}$ 1/K. As a result, a temperature change of 100 K leads to a relative size mismatch of about 1%, so one often needs to use some additional fixation tools to keep metal and polymer parts together. A relevant example is the fixation of an automobile bumper on a car's body where, on a base of 2 m, the unconstrained size mismatch reaches 2 cm as the temperature changes by a hundred degrees.

Many fibers have a very low or even negative thermal expansion in the fiber direction. Therefore, one is interested in putting short fibers into a polymer in order to obtain a material with a lower effective thermal expansion. In this study, the goal is to match the longitudinal thermal expansion of a polymer-based composite with that of aluminum. For this, we consider a composite of perfectly aligned, randomly situated carbon fibers and, for computer models with 16 fibers, carry out numerical predictions of the effective thermal expansion coefficients. Here our interest is in relatively small fiber volume fractions, where the composite can still maintain the attractive mechanical, impact, insulation, and other properties of unfilled organic polymers.

Figure 10 demonstates that the Halpin−Tsai equation considerably underestimates the technological potential of short-carbon-fiber-reinforced polymers, leading one to the wrong perspective about the attainability of maximal performance.

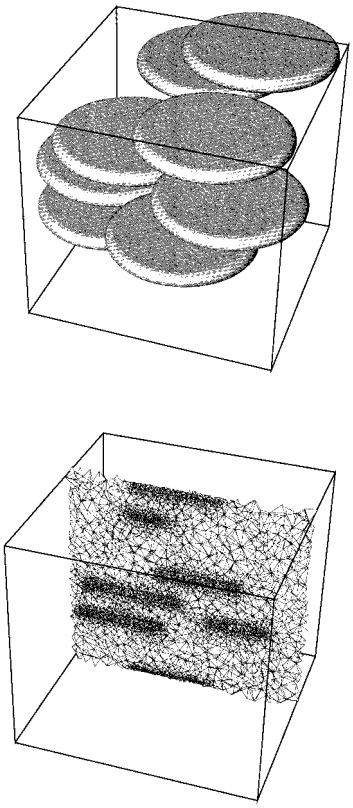

Figure 11. Periodic computer model with nine randomly situated identical disks of an aspect ratio of 10. The disk volume fraction is $f = 0.05$. The starting regular configuration consisted of a vertical stack of nine equispaced coaxial disks. Accordingly, orthorhombic periodic boundary conditions were set by an orthorhombic box with the edges scaled as 1:1:0.9, with the latter direction being the vertical one. A Monte Carlo run of a million steps was then carried out, keeping the disk orientations unchanged. The final random configuration was taken for numerical analysis. Its sketch is shown in the figure. The periodic morphology−adaptive quality mesh generated for this random Monte Carlo model had about 2×10^5 nodes and 10^6 tetrahedra.

Platelet-Reinforced Polymers

Computer Models. We have used three-dimensional periodic computer models consisting of a random dispersion of nonoverlapping identical parallel disks (see object B in Figure 1). Starting from regularly packed initial configurations, Monte Carlo runs were carried out to generate random configurations. Orthorhombic periodic boundary conditions were imposed. For a model with a single disk, the box aspect ratio was made the same as that of the disk. For a multiinclusion model, the box edges were scaled in each direction, proportional to the number of the disks in this direction. Figure 11 presents one of the computer models employed below for the numerical modeling of the dimensional stability of a platelet-reinforced glassy polymer.

For the matrix we assumed some typical elastic parameters of a glassy polymer, namely a Young's modulus of $E_m = 3$ GPa and a Poisson's ratio of $\nu_m = 0.35$. For the stiff reinforcing platelets, we assumed an isotropic behavior with a Young's modulus $E_f = 100$ GPa and Poisson's ratio $\nu_f = 0.2$. These parameters would be typical of a number of different inorganic fillers including silica, hydroxyapatite, and talcum.

Dimensional Stability of a Platelet-Reinforced Glassy Polymer. Glassy polymers like polycarbonates have traditionally been used in many demanding applications, including data storage on compact disks. However, because of intrinsic physical aging, possible water uptake, or the presence of residual stresses, some size and shape relaxation gradually takes place, typically resulting in distortions with a strain on the scale of a fraction of a percent or so in the year after manufacture.

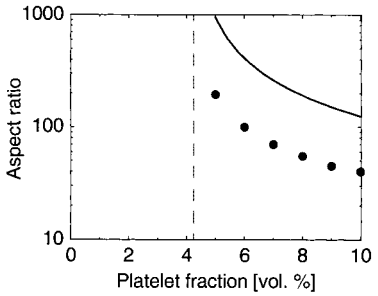

Figure 12. Design curve for a platelet-reinforced glassy polymer with a 5-fold increased dimensional stability. Numerical predictions are shown by solid circles. They were obtained from calculated aspect ratio dependences at different fixed disk volume fractions. Periodic models comprised of nine randomly situated parallel disks (see Figure 11) were used in calculations. The vertical dashed line shows the effect that can be achieved with disks of an infinite aspect ratio, i.e., assuming a layered, lamella-like morphology.

Here we would like to check to see the extent to which one can improve the dimensional stability of glassy polymers by putting into them small fractions of rigid high-aspect ratio platelets. Our design goal is to lessen the size and shape distortions by a factor of 5. Formally, the shrinkage problem is identical to the thermal one, so the same numerical and analytical methodology can be employed.

Figure 12 presents numerical and Halpin−Tsai predictions on the dimensional stability. The difference between the two predictions is significant. For example, numerical results indicate that including about seven volume percent of platelets with an aspect ratio of about 50 would suffice for the 5-fold improvement in the dimensional stability. In contrast, the Halpin−Tsai equation suggests volume loadings of about 20% when dealing with platelets of the same aspect ratio. In many situations, such relatively high platelet loadings are unacceptable, not only because of the cost and processing considerations but also because of the likely degradation of the impact and other important material properties that commonly occur as the filler fraction increases.

Corollary. As we have seen, the Halpin−Tsai equation gives the wrong perspective for the potential of short-carbon-fiber- and platelet-reinforced polymers. Therefore, one should be cautious when using the empirical Halpin−Tsai equation to decide whether one can further improve the performance already seen with a given whisker- or platelet-reinforced polymer. It is numerical predictions obtained with well-controlled computer models that permit reliable identification of the potential of whisker- and platelet-reinforced polymers, thus allowing one to rationally navigate research, development, and investment in the field.

Void-Containing Polymers with a Low Dielectric Constant

Typically, solid organic polymers have dielectric constants between 4 and 5. However, in microelectronics, it is often desirable to have dielectric materials with a

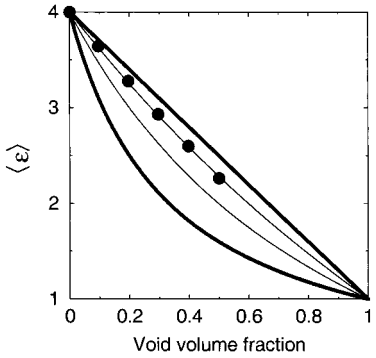

Figure 13. Effective dielectric constants of a polymer with spherical voids. Numerical predictions are shown by circles. They were obtained with periodic computer models comprised of a random dispersion of 27 nonoverlapping identical spherical voids. The two internal thin lines show the Hashin−Shtrikman bounds, while the two outside thick solid lines stand for Wiener's bounds.

lower dielectric constant. Air has a dielectric constant close to unity, so one can put some voids into a polymer to lessen its dielectric constant.

Bounds on the Effective Dielectric Constants. For a given void fraction, the variational Hashin−Shtrikman bounds establish rigorous upper and lower margins for the effective dielectric constant $\langle\epsilon\rangle$ of a macroscopically isotropic composite with inclusions of an arbitrary shape and size[15]

$$\epsilon_1 + \frac{f}{\frac{1}{\epsilon_2 - \epsilon_1} + \frac{1-f}{3\epsilon_1}} \le \langle\epsilon\rangle \le \epsilon_2 + \frac{1-f}{\frac{1}{\epsilon_1 - \epsilon_2} + \frac{f}{3\epsilon_2}} \qquad (34)$$

where ϵ_1 is the dielectric constant of the matrix, ϵ_2 the dielectric constant of the inclusion phase, i.e., for voids with $\epsilon_2 = 1$ in our case, and f the void volume fraction. Interestingly, for the composites with $\epsilon_2 < \epsilon_1$, the upper Hashin−Shtrikman bound duplicates the exact solution for the composite spheres model.[15] This solution was first obtained by Kerner for the electrical conductance.[47]

The dielectric constants of an anisotropic composite depend on the direction and they are not necessarily bounded by the Hashin−Shtrikman bounds. It is Wiener's bounds (essentially, predictions obtained assuming parallel and series connections of two infinite parallel layers) that specify the margins for the effective dielectric constants of anisotropic materials:

$$\frac{1}{\frac{1-f}{\epsilon_1} + \frac{f}{\epsilon_2}} \le \langle\epsilon\rangle \le (1-f)\epsilon_1 + f\epsilon_2 \qquad (35)$$

Wiener's bounds are generally considerably less restrictive than the Hashin−Shtrikman ones.

Spherical Voids. Figure 13 shows results obtained with computer models comprised of a random dispersion of identical non-overlapping spherical voids (see Figure 2). Periodic morphology−adaptive quality meshes were employed in the calculations (see Figure 3). One can see that numerical predictions practically follow the upper Hashin−Shtrikman bound, the worst possible scenario for an attempt to lessen the effective dielectric constant of a macroscopically isotropic composite. Moreover, because of the relatively small difference in the phase dielectric constants, the upper and lower Hashin−Shtrikman bounds are quite tight, so that little further can be gained by varying the geometric parameters of the voids, provided that the composite still remains macroscopically isotropic. All in all, macroscopically isotropic voided polymers, especially ones with spherical voids, are poorly suited for reducing the effective dielectric constants.

In microelectronics, one usually uses polymer materials in a form of thin films with the electric field applied perpendicular to the film plane. As a result, one is interested in a low dielectric constant in the direction perpendicular to the film plane and is not concerned much about the dielectric constants in the lateral directions. As can be seen from Figure 13, Wiener's bounds applicable for this anisotropic case are much less restrictive than the Hashin−Shtrikman ones. Which morphologies can deliver the effective dielectric constants close to the lower Wiener bound?

Biaxially Drawn Voided Films. Biaxial drawing is a traditional technological route employed for obtaining thin polymer films.[48] Here, we assume that the biaxial drawing of a voided polymer occurs by means of an affine deformation at constant volume. In this case, originally spherical voids turn into ellipsoidal ones with aspect ratios of λ:λ:$(1/\lambda^2)$, where the latter term represents the direction perpendicular to the film plane and λ is the draw ratio (see objects A and C in Figure 1).

As $\lambda \to \infty$, the morphology starts to resemble a lamella-like one, allowing one to surmise that the effective dielectric constant perpendicular to the draw plane should somehow decrease toward the lower Wiener's bound realizable in a composite of infinite parallel lamellas. Nonetheless, the limiting morphology developed as $\lambda \to \infty$ is different from the lamella-like one, so the limiting dielectric constants may also differ from Wiener's predictions.

We begin with computer models comprised of 27 nonoverlapping identical spherical voids randomly dispersed in cubic boxes under periodic boundary conditions (see Figure 14). These systems correspond to a draw ratio of $\lambda = 1$. To generate a model for $\lambda > 1$, we impose an affine transformation to yield an orthorhombic periodic box with the edges scaled as λ:λ:$(1/\lambda^2)$. Simultaneously, we scale accordingly the center-of-mass coordinates of the spheres and replace them by ellipsoidal inclusions of the same aspect ratios as those of the periodic box (see Figure 14). The so-obtained periodic models are meshed and the resulting periodic morphology−adaptive quality meshes are used for numerical predictions of the effective dielectric constants as functions of the draw ratio λ.

Figure 15 presents numerical results obtained for a voided polymer with a void volume fraction of 0.3. One can see that, at relatively small draw ratios, the effective dielectric constants are quite sensitive to the draw ratio. Therefore, in this domain of small draw ratios, one can sensibly control the effective dielectric constants by changing the draw ratio. Interestingly, already at $\lambda \approx 1.5$, the normal, out-of-plane component ϵ_z becomes smaller than the lower Hashin−Shtrikman variational bound. The leveling off occurs at $\lambda \approx 3$ where the effective dielectric constants become practically independent of the further increase in the draw ratio. On the plateau, the lateral, in-plane dielectric constants approach the upper Wiener's bound while the normal one is stationary at $\epsilon \approx 2.45$. The latter value is roughly in the middle between the value $\epsilon \approx 2.9$ obtained with spherical voids and the lower Wiener's bound, i.e., $\epsilon \approx 2.1$.

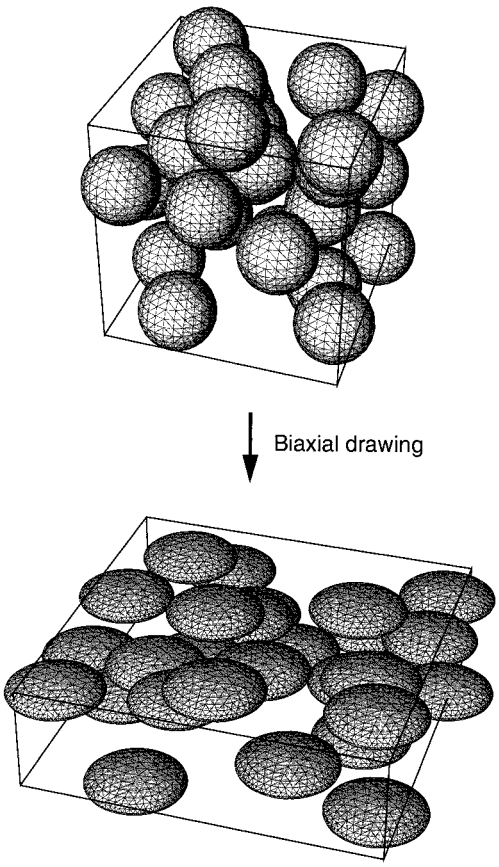

Figure 14. Generation of computer models for biaxially drawn voided polymers. The sketches illustrate the drawing of a voided polymer with a void volume fraction of $f = 0.3$. The draw ratio $\lambda = 1.5$. Note that curvature-adaptive surface meshes are employed for the spheroidal inclusions.

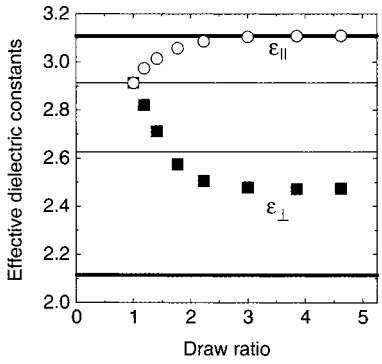

Figure 15. Effective dielectric constants of biaxial drawn voided films. The two internal thin lines show the Hashin–Shtrikman bounds, while the two outside thick solid lines stand for Wiener's bounds. For an affine drawing, the draw ratio λ and the aspect ratio a of a drawn spheroidal void are related as $a = \lambda^3$.

Corollary. As has already been reviewed in Table 1, apart from the effective dielectric constants, Laplace's equation is also applicable for a number of other technological properties of multiphase materials. As two immediate examples, Laplace's solver and the models just used above for the numerical identification of voided polymers with a low dielectric constant can readily be used to check to see numerically whether the same voided films can exhibit some interesting thermal insulation properties, or whether biaxially drawn films of block-copolymers can offer an attractive combination of oxygen/nitrogen selectivity and permeability coefficients.

Conclusions and Perspectives

We presented a numerical finite-element-based methodology for predicting the effective properties of multiphase materials. A distinct feature of the approach is a consistent use of periodic boundary conditions in the course of generating random multiinclusion Monte Carlo configurations, tessellating them into morphology–adaptive quality meshes, and numerical solution for the effective properties. The approach is exact in principle and efficient in practice, allowing one to predict the behavior and properties of actual multiphase materials based on remarkably small computer models. In the application examples considered, we identified numerically some whisker- and platelet-filled polymers with tailored elastic, thermal, and dielectric properties. It appeared that the widely used Halpin–Tsai equation systematically and considerably underestimates the actual potential of whisker- and platelet-reinforced polymers. As a consequence, in the search for advanced multiphase materials, one should rely rather on numerical predictions obtained with well-controlled computer models.

It is commonly believed that boundary-element methods should be most effective for numerical predictions of the behavior and properties of multiphase materials.[49–51] However, considering the absence of closed-form Green's functions for generally anisotropic elastic media, the unfavorable, quadratic memory requirements for the storage of the fully populated matrices intrinsic to the nonlocal BEM formulations, as well as the necessity of carrying out quite demanding long-range corrections for periodic systems, one should take rather a cautious attitude regarding the claimed superiority of BEM methods. Indeed, here we presented generally anisotropic periodic local formulations resulting in sparse stiffness matrices with the total number of nonzero elements scaling linearly with the system size. Intrinsically, no long-range corrections were needed for periodic systems. On the basis of morphology–adaptive quality meshes, we studied representative periodic computer models comprised of a dozen or more high-aspect-ratio whiskers or platelets randomly dispersed in a polymer. Remarkably, all calculations presented in this paper were carried out on a workstation, in a favorable distinction to a recently reported BEM study on a 1840-processor parallel supercomputer.[50]

In this paper, we have focused on the linear-response properties of whisker- and platelet-filled polymers. However, the numerical approach presented is generic, signifying that one can readily use it for predicting linear-response properties of three or more phase composite materials comprised of anisotropic, arbitrarily shaped and oriented phases, including nanocomposites of complex microstructure and various compound materials. The approach is now being extended to composites with complex co-continuous morphologies frequently occurring in immiscible polymer blends and block copolymers,[52–54] as well as to large-strain rate-dependent deformations typical of plastic, impact, and flow responses of polymers and polymer-based composites.

Putting things in perspective, the properties of a single-phase, homogeneous material can be predicted from its chemical composition, by means of a group-contribution method or a molecular simulation with an atomistically detailed computer model. The properties of a multiphase, heterogeneous material are not uniquely determined by the chemical composition while molecular

simulations are usually impractical, because of the large representative volume element size for the complex morphologies typical of most advanced materials. The continuum approach presented in this paper allows the rational prediction of properties for multiphase materials from those of each phase and the morphology, thus complementing the molecular-level methods used for predicting the properties of single-phase materials.

Acknowledgment. The work presented is a continuation of the original Habilitation dissertation defended by the author in the Department of Materials at ETH Zürich. I am grateful to the faculty members for the favorable consideration given to my dissertation. I very much thank Professor U. W. Suter of ETH Zürich for many stimulating discussions, his advice, encouragement, and help in many ways. My thanks also go to Professor I. M. Ward of IRC in Leeds. Interacting with him has been a most gratifying and stimulating experience. I thank Dr. M. G. Rozman of ETH Zürich for his contribution in the development of principles of generating periodic morphology−adaptive quality meshes. I am also thankful to Dr. A. H. Widmann-Schupak of MatSim GmbH for many discussions and his involvement in commercial implementation[55] of the numerical algorithms presented in this paper.

References and Notes

(1) Citation Database of the Institute for Scientific Information, http://wos.isiglobalnet.com.
(2) Dagani, R. *Chem. Eng. News* **1999**, June 7, 25−37.
(3) Calvet, P. *Nature* **1999**, *399*, 210−211.
(4) Kurauchi, T.; Okada, A.; Nomura, T.; Nishio, T.; Saegusa, S.; Deguchi, R. *SAE Tech.l Pap. Ser.* **1989**, No. 910584.
(5) Favier, V.; Chanzy, H.; Cavaillé, J. Y. *Macromolecules* **1995**, *28*, 6365−6367.
(6) Jin, L.; Bower, C.; Zhou, O. *Appl. Phys. Lett.* **1998**, *73*, 1197−1999.
(7) Dufresne, A.; Kellerhals, M. B.; Witholt, B. *Macromolecules* **1999**, *32*, 7396−7401.
(8) Dubief, D.; Samain, E.; Dufresne, A. *Macromolecules* **1999**, *32*, 5765−5771.
(9) Brinker, C. J.; Lu, Y.; Sellinger, A.; Fan, H. *Adv. Mater.* **1999**, *11*, 579−585.
(10) Ginzburg, V. V.; Singh, C.; Balazs, A. C. *Macromolecules*, **2000**, *33*, 1089−1099.
(11) Seki, T.; Kojima, J.; Ichimura, K. *Macromolecules* **2000**, *33*, 2709−2717.
(12) Huang, L. R.; McMillan, R. A.; Apkarian, R. P.; Pourdeyhimi, B.; Conticello, V. P.; Chaikof, E. L. *Macromolecules* **2000**, *33*, 2989−2997.
(13) Limary, R.; Swinnea, S.; Green, P. F. *Macromolecules* **2000**, *33*, 5227−5234.
(14) Christensen, R. M. *Mechanics of Composite Materials*; Krieger Publishing Co.: FL, 1991.
(15) Hashin, Z.; Shtrikman, S. *J. Appl. Phys.* **1962**, *33*, 3125−3133.
(16) Hashin, Z.; Shtrikman, S. *J. Mech. Phys. Solids* **1963**, *10*, 335−342.
(17) Miller, M. N. *J. Math. Phys.* **1969**, *10*, 1988−2009.
(18) Walpole, L. J. *J. Mech. Phys. Solids* **1969**, *7*, 235−251.
(19) Willis, J. R. *Adv. Appl. Mech.* **1981**, *21*, 85−202.
(20) Willis, J. R. *J. Mech. Phys. Solids* **1991**, *39*, 73−86.
(21) Hashin, Z. *J. Appl. Mech.* **1983**, *50*, 481−505.
(22) Halpin, J. C. *J. Composite Mater.* **1969**, *3*, 732−747.
(23) Halpin, J. C.; Kardos, J. L. *Polym. Eng. Sci.* **1976**, *16*, 344−352.
(24) Hull, D. *An Introduction to Composite Materials*; Cambridge University Press: Cambridge, England, 1981.
(25) Agarwal, B. D.; Broutman, L. J. *Analysis and Performance of Fibre Composites*; Wiley: New York, 1990.
(26) Tucker, C. L.; Liang, E. *Composites Sci. Technol.* **1999**, *59*, 655−671.
(27) Gusev, A. A. *J. Mech. Phys. Solids* **1997**, *45*, 1449−1459.
(28) Huet, C. *J. Mech. Phys. Solids* **1990**, *38*, 813−841.
(29) Hazanov, S.; Huet, C. *J. Mech. Phys. Solids* **1994**, *42*, 1995−2011.
(30) Drugan, W. J.; Willis, J. R. *J. Mech. Phys. Solids* **1996**, *44*, 497−524.
(31) Goussev, O. A.; Richner, P.; Rozman, M. G.; Gusev, A. A. *J. Appl. Phys.* **2000**, *88*, 4013−4016.
(32) Delaunay, B. N. *Izv. Akad. Nauk SSSR, VII ser., Otd. Mat. Estest. Nauk* **1934**, *7*, 793−799.
(33) Bowyer, A. *Comput. J.* **1981**, *24*, 162−166; Watson, D. E. *Comput. J.* **1981**, *24*, 167−177.
(34) Bern, M.; Eppstein, D. *Comput. Euclidean Geom.*, **1992**, *1*, 23−90.
(35) Mavriplis, D. J. *Annu. Rev. Fluid Mech.* **1997**, *29*, 473−506.
(36) Shewchuk, J. R. Delaunay Refinement Mesh Generation. Ph.D. Thesis, School of Computer Science, Carnegie Mellon University, Pittsburgh, PA, 1997. Available as Technical Report CMU-CS-97-137.
(37) Widmann-Schupak, A. H. Private communication, MatSim GmbH, Zürich, Switzerland.
(38) Frey, W. H. *Int. J. Numer. Methods Eng.* **1987**, *24*, 2183-2198.
(39) Shewchuk, J. R. *Discrete Comput. Geom.* **1997**, *18*, 305−339.
(40) Hale, D. K. *J. Mater. Sci.* **1976**, *11*, 2105−2187.
(41) Landau, L. D.; Lifshitz, E. M. *Electrodynamics of continuous media*; Pergamon Press: Oxford, England, 1984.
(42) Zienkiewicz, O. C.; Taylor, R. L. *The Finite Element Methodology*, 4th ed.; McGraw-Hill: London, 1990.
(43) Gusev, A. A.; Hine, P. J.; Ward, I. M. *Composites Sci. Technol.* **2000**, *60*, 535−541.
(44) Landau, L. D.; Lifshitz, E. M. *Theory of elasticity*; Pergamon Press: Oxford, England, 1984.
(45) Saad, Y. *Iterative Methods for Sparse Linear Systems;* PWS Publishing Co.: Boston, MA, 1996.
(46) Hine, P. J. Private communication. Interdisciplinary Research Center, Leeds, U.K.
(47) Kerner, E. H. *Proc. Phys. Soc.* **1956**, *B69*, 802−817.
(48) Ward, I. M. *Mechanical Properties of Solid Polymer*, 2nd ed.; Wiley: Chichester, England, 1983.
(49) Greengard, L.; Hesling, J. *Rep. Courant Mater. Comput. Lab.* **1997**, *97*, 1−22.
(50) Ingber, M. S.; Papathanasiou, T. D. *Int. J. Numer. Methods Eng.* **1997**, *40*, 3477−3491.
(51) Phan-Thien, N.; Kim, S. *Microstructures in Elastic Media: Principles and Computational Methods;* Oxford University Press: New York, 1994.
(52) Bates, F. S.; Fredrickson, G. H. *Phys. Today* **1999**, *52*, 32−38.
(53) Drolet, F.; Fredrickson, G. H. *Phys. Rev. Lett.* **1999**, *83*, 4317−4320.
(54) Heier, J.; Kramer, E. J.; Groenewold, J.; Fredrickson, G. H. *Macromolecules* **2000**, *33*, 6060−6067.
(55) *Palmyra*. Materials Simulation GmbH, Zürich, Switzerland, http://www.matsim.ch.

MA001979B